The perpetual shearing of granular soils under low stresses using the stadium shear device

Yang Liu [a], **François Guillard** [a], **Benjy Marks** [a], **Pierre Rognon** [a] **& Itai Einav** [a]

[a] *Particles and Grains Laboratory, School of Civil Engineering, The University of Sydney, Australia.*
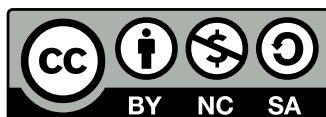
Abstract. The constitutive response of granular soils under indefinitely large shear deformation and low stress controls the dynamics of shallow landslides and offshore pipelines. Current testing devices, however, are either limited to small shear deformation or involve a non-uniform stress distribution across the sample being tested. This paper presents the development of an original stadium shear device (SSD) that is free from those issues. In the SSD, soil samples can deform perpetually within a closed stadium shaped container that is sheared continuously by a belt. The stress uniformity across the width of the device is validated using Discrete Element Method (DEM) simulations, which give insight into the relationships between the normal stresses acting on the material. The performance of the SSD is validated using experimental data obtained from tests on glass beads, which further disclose stress and void ratio relationship in soils. When applied to sub-angular natural sands with different degrees of polydispersity, the SSD reveals a weak rate hardening of friction coefficient and sample dilatancy that reaches the loosest possible density at critical state, regardless of the initial packing conditions.

Keywords. Sand, Shear, Elementary tests, Low stress, Critical state

1. Introduction

The shear response of granular soils is one of the key factors determining landslide dynamics. Shallow landslides at relatively low stress occur on steep mountain hillslopes as a form of topographic relief through shear-induced fluvial and glacial erosion [Larsen et al., 2010, Rood, 1984, Wilford and Schwab, 1982]. The shear response of soils at low stress is also important for predicting the movement of pipelines on the seabed [Tian and Cassidy, 2008, White et al., 2007, Zhang et al., 2002] and the general response of extraterrestrial soils under low gravity [Carrier et al., 1991, Mitchell et al., 1972]. It is widely known that under low stresses, where grain crushing does not noticeably develop [Bandini and Coop, 2011, Tengattini et al., 2016], the critical state of sheared granular soils can be described in terms of density and stress in a way that is mostly independent of the initial density and stress [Bolton, 1986, Negussey et al., 1988, Rousé, 2018, Schanz and Vermeer, 1996, Vaid and Sasitharan, 1992]. Understanding this stress-strain-density relationship at critical state requires experimental techniques that can operate under perpetual shear conditions and low stresses. However, most conventional shear testing techniques in geotechnical engineering such as the shear box, biaxial and triaxial shear cells, and the true triaxial device, are limited to small deformations that often produce strain rate heterogeneities that distort the shape of soil samples. Subsequently, using such devices for the determination of large-strain critical state behaviour is often done through extrapolation from limited small strain data.

In order to resolve this issue of insufficient shear strain development during testing, Hvorslev [1936, 1939] introduced the ring shear device for soil testing under large shear deformation, where one annulus rotates above a second annulus. The key point of its cylindrical geometry is the ability to shear the soil perpetually without changing the overall geometry, as the flow in the cylinder follows a closed path. This configuration has been widely employed [Bishop et al., 1971, Bosdet, 1980, Bridgewater, 1972, Kelly et al., 2003, Miller et al., 1996, Negussey et al., 1988, Novosad, 1964, Sassa, 1997, Savage and Sayed, 1984, Tabucanon, 1997] to study the shear response of granular soils. Another way to establish a perpetual cylindrical flow is through the use of a Couette device, where the sample is sheared by rotating either the inner or outer cylinder of the same geometry [Bocquet et al., 2001, Chambon et al., 2003, Cheng et al., 2006, Fenistein et al., 2004, Howell et al., 1999, Khosropour et al., 1997, Losert et al., 2000, Mueth et al., 2000, Veje et al., 1999]. Both the ring shear and Couette testing devices are cylindrical geometries and therefore impose a radially-dependent non-uniform stress field. This is known to lead to the underestimation of the measured shear stresses and the development of secondary flows [Savage and Sayed, 1984] during shearing. One way to minimise this issue of radial stress dependence is to increase the ring's diameter, sometimes even beyond one metre, using the so-called large ring shear apparatus [Kelly et al., 2003, Tabucanon, 1997]. The operation of such large ring shear devices is

inevitably demanding and energy consuming, while not entirely resolving the radial dependence.

Another remarkable configuration is the "caterpillar shear device" of Allersma [1987], which avoids the radial dependence of stress and enables only finite yet high shear deformation up to 60% nominal shear strain. The device has significant similarities to the perpetual shear device proposed here, in that the material is confined within a flexible belt. Additionally, the use of crushed glass particles and refractive index matched oil allowed for in-situ measurements of the stress field. The device enables control over two degrees of freedom of stress/strain control (shear strain and normal stress on the shear plane).

In order to avoid the radial dependence of stress, while imposing infinite shear deformation and allowing three degrees of freedom of stress/strain control, the "stadium shear device" (SSD) was recently patented for the testing of both disk systems in 2D and granular soils in 3D configurations [Einav et al., 2014]. The 2D configuration was successfully constructed and used to inspect the internal kinematics of disks during perpetual shear using image analysis and particle tracking [Miller et al., 2013, Rognon et al., 2015a, Sun et al., 2020], but the 3D configuration has never been implemented before. The purpose of the current paper is to present the development and construction of the first working 3D SSD prototype for natural granular soil testing under low and assumed uniform stresses in perpetual shear conditions. Here, the 3D SSD will be used on various granular samples such as glass beads and sand, whilst varying the imposed stresses and shear rates.

This paper begins by detailing the newly established 3D SSD in terms of its dimensions, stress and strain conditions, and the techniques used to minimise intrinsic friction along its boundaries. The calibration and experimental techniques developed are then outlined. The accuracy of the device is next cross-validated by comparing the behaviour of the system when applied to glass beads against simulations using the Discrete Element Method (DEM). These simulations are also used to confirm the existence of stress uniformity across the rectangular section of the 3D SSD. Detailed investigation of the effects of grain size and shape, grain size distribution, initial density, and shear rate on the response of granular soils under perpetual motion and low vertical stress conditions are then carried out and analysed in terms of dilation and the evolution of the friction coefficient towards true critical state. A particular focus is given to inspecting strain rate sensitivity at low rates for both glass beads and sand samples, and while no such sensitivity is found in glass beads, a mild strain rate hardening is found in sand.

2. 3D Stadium Shear Device

2.1. Prototype

Fig. 1(a) shows a schematic diagram of the 3-Dimensional SSD prototype developed for this paper. The configuration enables the application of arbitrarily large shear deformation under constant vertical normal stress and constant

Yang Liu, François Guillard, Benjy Marks, Pierre Rognon & Itai Einav, *The perpetual shearing of granular soils under low stresses using the stadium shear device*

horizontal normal strain conditions, and the measurement of the normal and shear stresses acting on the shearing belt. The shearing belt is customised from a commercially available timing belt (Bando HTS 966-14M). The belt is flat (i.e. having no teeth) from the bottom to above the level of the top loading plate in order to allow the loading plate to move freely and prevent leakage of particles, and to sit within the Teflon U-shaped grooves in the base plate, again to prevent particle leakage. Above the loading plate, the belt has teeth to engage with the driving and idle sprockets. The belt was placed centrally inside a confining case (540 mm length×250 mm width×190 mm height) which supports the external power and measurement devices. Powered by a motor (GPG 90mm geared AC speed control motor, model 5IK120RHU-C) and gear assembly concentrically installed on top of the driven sprocket (diameter d = 124 mm), the belt can operate at shear velocities from 0.787 ~ 78.7 mm/s. An idler sprocket is positioned on the other end of the belt as indicated in Fig. 1(c), which ensures that the belt forms a stadium-like cross section in plan view. The test material is placed inside the belt, and is vertically confined by a top plate as indicated in Fig. 1(b). A vertical rod is connected to the top plate to allow for the application of a vertical confining stress on the sample. To avoid tilting, the vertical rod is guided by a linear roller bearing, shown in Fig. 1(c), which is attached to the confining case. In this way, the top plate applies a constant vertical stress to the sample, which can compress or dilate freely in the vertical direction. The displacement of the top plate was monitored by a linear variable differential transformer (LVDT) sensor during testing to measure the change of height of the sample.

Horizontally, the belt is confined by two side plates of length 175 mm and height 100 mm, imposing zero lateral normal strain. The horizontal normal forces on these plates are measured using two load cells (Mark-10 MR01-100#) as indicated in Fig. 1(b). The test material is filled above the side plate (h > 100 mm) to ensure the horizontal normal forces F_N are accurately measured. The torque $\mathcal{M}$ and rotation rate are recorded from a torque transducer (Kistler 4520A050, range: 50 N.m) coaxially installed under the motor and gearbox assembly. The measurement of the torque on the motor allows for the calculation of the shear force that the belt applies to the specimen.

Four strategies were implemented to prevent small particles from leaking through the gaps between the belt and the upper and lower plates: (1) The belt was placed inside a U-shaped groove on the base plate in order to stop particles escaping from underneath the belt. The groove configuration also helps minimising belt deformation during shear; (2) All the teeth on the belt below the sprocket level were removed to minimise the gap between the belt and the top plate; (3) Two layers of brush-like draught excluder (Raven R61) were glued along the side boundary of the top plate to stop particles escaping upwards through the gap, while also reducing unwanted friction; and (4) the typical grain size in all the experiments was selected to be above 1 mm in order to minimise the occurrence of leaks.

Three techniques were implemented to minimise unwanted friction between moving components: (1) At the bottom plate, the U-shaped groove guiding the belt was made out of a Teflon sheet with a low friction coefficient; (2) On the top plate, the brush-like draught excluder is highly compliant which also reduces friction; (3) The contact between the side plates, which are used to impose zero lateral normal strains, and the belt was made through roller bearings to minimise friction along the shear direction of the belt.

2.2. Stress tensor measurement

The representative stress tensor of an element of the tested material is portrayed in Fig. 2. For this geometry, the average frictional stress component on the horizontal planes can be neglected ($\tau_{zx} = \tau_{zy} = 0$) due to the distribution of the local frictional stresses on that plane, which is expected to be anti-symmetric about the longitudinal central axis. It then follows from equilibrium that the frictional stress components directed vertically can also be neglected ($\tau_{xz} = \tau_{yz} = 0$). The four remaining non-zero stress components defining the stress state in the 3D SSD can be calculated as follows:

(1) The vertical normal stress σ_{zz} is calculated as the overall vertical normal force divided by the horizontal plate-soil contact area. The overall vertical normal force F_N is given by the applied vertical normal force plus the vertical stress contribution to the middle of the sample from the self-weight of the particles.

(2) The lateral normal stress σ_{xx} is calculated as

$$\sigma_{xx} = \frac{\alpha(F_N - F_{N0})}{lh}, \tag{1}$$

where l = 395 mm is the projected longitudinal length of the belt (as indicated in Fig. 2), h the sample height, F_{N0} the force measured when the system runs freely without test material, and α a factor to correct for the fact the lateral load from the sample is only partly transferred to the load cells due to the bottom groove and sprockets. The calibration of α will be detailed in the *Calibration procedure*, section 3.1, along with a discussion on potential issues and scope for improvement.

(3) The other normal lateral stress σ_{yy} can not be measured directly during the experiments. However, using the DEM model described below it will be shown that it is generally equal to σ_{xx}.

(4) The in-plane shear stress $\tau_{xy} = \tau_{yx}$ can be calculated by assuming a uniform distribution along the belt and moment equilibrium:

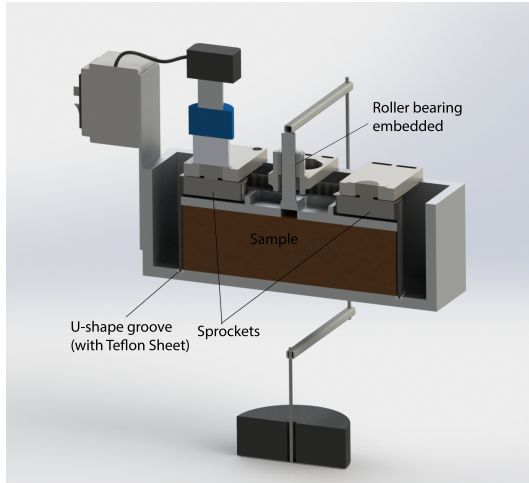$$\tau_{xy} = \frac{\mathcal{M} - \mathcal{M}_0}{RhL}, \tag{2}$$

where $\mathcal{M}$ is the applied torque, R the radius of the sprockets, L = 966 mm the overall length of the belt, and $\mathcal{M}_0$ the non-zero applied torque found when the system runs without the sample. Several potential measurement issues and scope for improvement will be discussed in section 3.1.
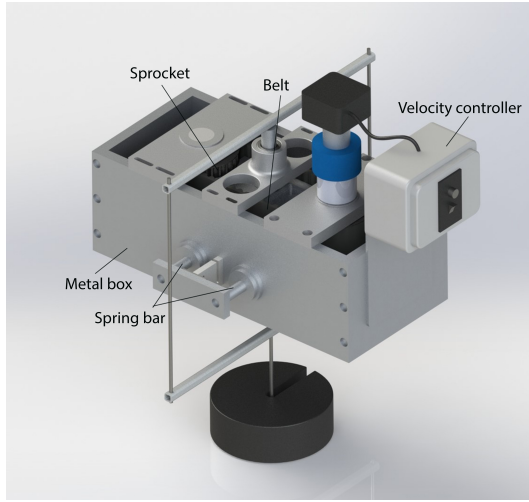
(a)
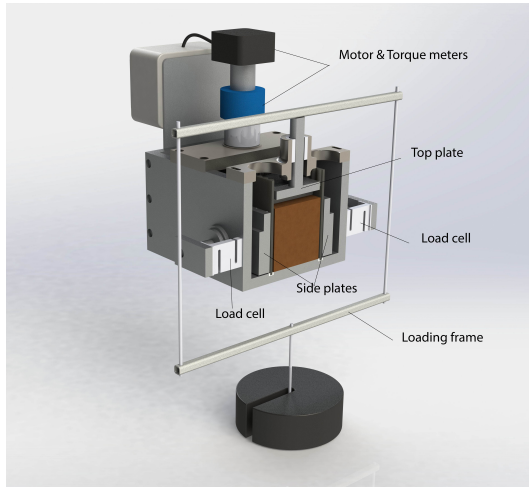
(b)

(c)

Figure 1. Schematics of the 3D stadium shear device (3D SSD), (a) overview; (b,c) vertical cross sections
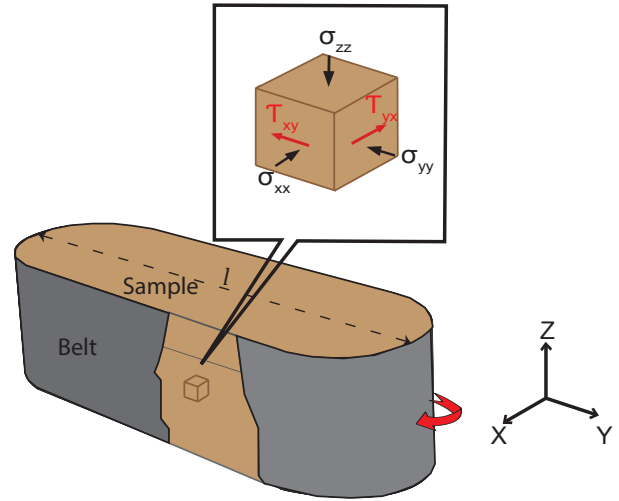

Figure 2. Schematic diagram of the four stress components acting on a material element in the central region of the sample ($\tau_{xy} \equiv \tau_{yx}$ from equilibrium).

2.3. Stress ratios

The stress state is further analysed using Mohr circles diagrams corresponding to representative volume elements. Given the four stress components stated above, the dimensionality of the problem requires three distinct Mohr circles. Three stress ratios can be defined from the four independent stress components:

$$\mu = \frac{\tau_{xy}}{\sigma_{xx}}, \quad k = \frac{\sigma_{xx}}{\sigma_{zz}}, \quad s = \frac{\sigma_{yy}}{\sigma_{xx}}. \tag{3}$$

While μ and k are directly measurable in the current configuration, s is not. However, it will be shown in section 2.5 using DEM simulations that $s \approx 1$ for spherical grains, but for generality here we keep s as an unknown. Since σ_{xx} and σ_{yy} act on orthogonal planes, the line that joins their points (σ_{xx}, τ_{xy}) and (σ_{yy}, τ_{yx}) passes through the centre of the r-radius Mohr's circle of the horizontal xy plane (with normal in z direction) given by $(\sigma_m, 0)$ with

$$\sigma_m = \frac{\sigma_{xx}}{2}(1+s), \quad r = \frac{\sigma_{xx}}{2}\sqrt{(1-s)^2 + 4\mu^2}. \tag{4}$$

In terms of the principal stresses, two ratios can be defined, corresponding to a Rankine-like earth pressure coefficient and a friction coefficient:

$$k_{13} = \frac{\sigma_1}{\sigma_3}, \quad \phi = \arcsin\left(\frac{\sigma_1 - \sigma_3}{\sigma_1 + \sigma_3}\right). \tag{5}$$

Given the condition of zero shear stress along the horizontal xy plane, the vertical normal stress σ_{zz} is a principal stress (see Fig. 3). Whether σ_{zz} is the maximum σ_1 (Fig. 3(a)), intermediate σ_2 (Fig. 3(b)) or minimum principal stress σ_3 (Fig. 3(c)) depends on whether it is larger, smaller or in-between the other two principal stresses, a condition that may in general even change during the test. The expressions for k_{13} and ϕ for these three corresponding options are listed below:
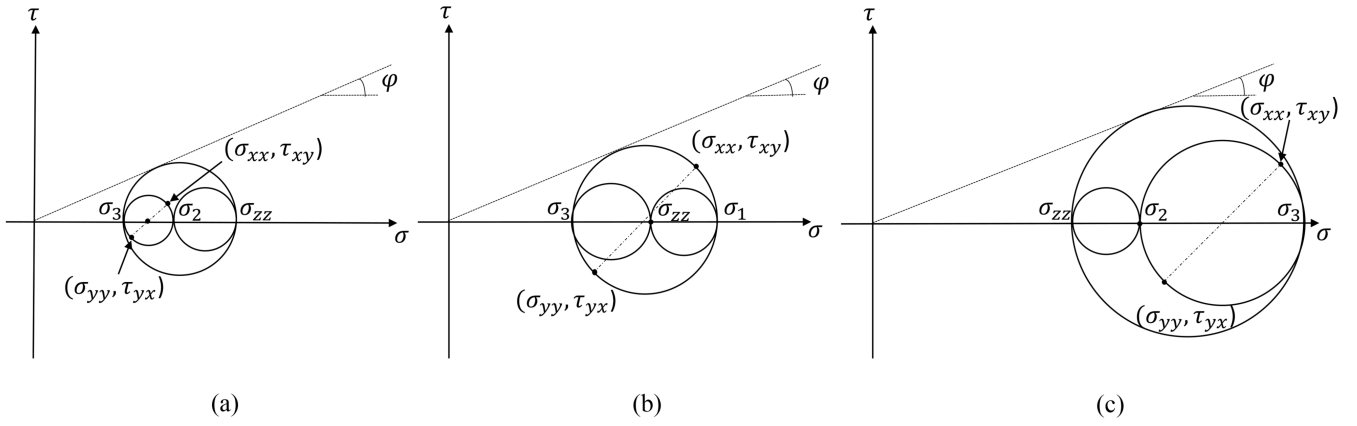
Figure 3. Stress representations using Mohr's circles for three cases: (a) σ_{zz} σ_1, (b) σ_{zz} σ_2, (c) σ_{zz} σ_3.

(1) The case of $\sigma_{zz} = \sigma_1$ occurs when $\sigma_{zz} \geqslant \sigma_m + r$, as shown in Fig. 3(a). In this case, we find:

$$k_{13} = \frac{2}{k\left(1 + s - \sqrt{(1-s)^2 + 4\mu^2}\right)}, \qquad (6)$$

$$\phi = \arcsin\left(\frac{2 - k\left((1+s) + \sqrt{(1-s)^2 + 4\mu^2}\right)}{2 + k\left((1+s) - \sqrt{(1-s)^2 + 4\mu^2}\right)}\right). \qquad (7)$$

(2) The case of $\sigma_{zz} = \sigma_2$ occurs when $\sigma_m - r \leqslant \sigma_{zz} < \sigma_m + r$, as shown in Fig. 3(b). In this case:

$$k_{13} = \frac{(1+s) + \sqrt{(1-s)^2 + 4\mu^2}}{(1+s) - \sqrt{(1-s)^2 + 4\mu^2}}, \qquad (8)$$

$$\phi = \arcsin\left(\frac{\sqrt{(1-s)^2 + 4\mu^2}}{1 + s}\right). \qquad (9)$$

(3) The case of $\sigma_{zz} = \sigma_3$ occurs when $\sigma_{zz} < \sigma_m - r$, σ_{zz}, as shown in Fig. 3(c). In this case:

$$k_{13} = \frac{k\left(1 + s + \sqrt{(1-s)^2 + 4\mu^2}\right)}{2}, \qquad (10)$$

$$\phi = \arcsin\left(\frac{k\left((1+s) + \sqrt{(1-s)^2 + 4\mu^2}\right) - 2}{k\left((1+s) - \sqrt{(1-s)^2 + 4\mu^2}\right) + 2}\right). \qquad (11)$$

Note that ϕ and k_{13} in either of the three cases listed above always depend on k, μ and s, but only k and μ are directly measurable in the current configuration. However, it will be demonstrated using the DEM model below that $s \approx 1$ for a system with spherical grains. Also, since the belt directly applies the shear stress components τ_{xy} and τ_{yx}, it is reasonable to assume that these components should belong to the biggest Mohr's circle. Therefore, the only valid solution is given by case 2 above.

2.4. Discrete Element model

Taking spherical particles as a reference case, a DEM model was developed in order to support the following assumptions for the SSD

(1) the stresses are distributed homoegeneously across the sample,
(2) the normal lateral stresses are equal (*i.e.*, $s = 1$),
(3) the effects of the roughness of the upper and lower planner boundaries on the measured material behaviour are minimal.

In addition, the DEM will further serve to cross-validate the physical tests in the case of sheared systems of spheres/glass beads.

The DEM model was executed using MercuryDPM [Thornton et al., 2012, Weinhart et al., 2012]. As shown in Fig. 4, the simulated model represents a slice of the system with width $w = 124$ mm, height approximately 110 mm and thickness 30 mm (10 grain diameters). Particles in the simulations represent 3 mm glass spheres with 20% polydispersity and a density of 2500 kg.m^{-3}. Contacts between the grains themselves and between grains and boundaries are modelled in the normal direction by linear spring-dampers, with stiffness and damping defined by a collision time of 88 µs and restitution coefficient of 0.5. Unless otherwise stated the contacts also have both sliding resistance, with particle-particle friction coefficient $\mu_s^p = 0.5$, and rolling resistance of $\mu_r^p = 10^{-3}$. These values have been previously measured experimentally and have been shown to well represent glass beads [Fuchs et al., 2014]. The system is bounded by rigid walls in the x and z directions, and is periodic in the y direction. The stress response was studied in terms of the dimensionless inertial number I, which is widely used in granular physics to represent frictional rate effects during granular flows in terms of the ratio between inertial and deformation timescales [da Cruz et al., 2005, MiDi, 2004, Savage, 1984]:

$$I = \dot{\gamma} d \sqrt{\frac{\rho}{p}}, \qquad (12)$$

where $\dot{\gamma}$ is the shear rate, $p = (\sigma_{xx} + \sigma_{yy} + \sigma_{zz})/3$ the mean stress, d the grain diameter, and ρ the grain density.

The walls represent the belt slide in the y direction and do not move in the x direction. Their rolling and sliding coefficients were set to unity, to limit particle sliding or rolling relative to the belt. The effect of the sliding coefficient μ_s of the grains with the top and bottom plates will be investigated, while fixing their rolling resistance to $\mu_r = 10^{-3}$. The top plate is allowed to move in the z direction, and is attached to a critically damped spring-damper system that applies a constant pressure. Particles are initially placed on a regular cubic grid in the space, and a relatively high $I = 0.1$

is first applied for a shear deformation of 1 mm to expedite the approach to critical state, together with the top load and gravity of 9.81 m.s^{-2}. After this stage, the shear rate is gradually lowered to achieve the targeted inertial number I. Once a steady state is reached (when the height of the top plate is relatively constant), the normal and tangential stresses on the boundaries are calculated, and averaged over 10 s of shearing. The total distance sheared is in the range of 0.005 to 30 m, depending on the case studied. To study the shear rate dependence of μ and k, further simulations were conducted under $I=10^{-3}$ and $I=10^{-4}$ for 14 mm glass beads when the grains to plates sliding coefficient μ_s was set to zero.

Like any DEM model, the one adopted in this paper also involves a variety of assumptions. For example, the contact between two spheres is best described by the non-linear Hertz law. In poly-disperse systems individual particles often involve many more contacts, and thus one can question the applicability of the Hertz law. Furthermore, in natural material particle roughness can often govern the observed relationship between the force and deformation at contacts. While these details are surely critical for determining bulk elasticity, their influence on the mobilised friction remains questionable. For these reasons we opt for simplicity and use linear contact laws. Nevertheless, future studies are recommended to explore these details in the context of the SSD that probe into these potential (likely second order) effects on the interpretation of the results.

Similarly, in general conditions granular flows would depend on at least one more dimensionless number in addition to the inertial number I. Specifically, where particle deformations at contact are relatively large compared to their radius, one should further consider the normalised pressure at contact by the contact stiffness over grain size squared. For the small pressures as those imposed in this paper the effect of this number is negligible, which makes the use of the soft-DEM in this study relevant and valid.

2.5. Steady state stress condition in DEM

In order to validate the first two assumptions listed above in Section 2.4, the stress distribution across the width of the 3D SSD device is analysed using the DEM model with $d = 3$ mm, $\mu_s = 0$ and $\rho = 2500$ kg/m^3. The shear rate was set for each case to achieve inertial numbers of $I=10^{-2}$ and 10^{-3} given imposed vertical stresses of $P =1000, 2000, 4000, 8000$ and 16000 Pa (10 simulations in total for this particle size). In Fig. 5(a) we report stress values in the sample at steady state, which have been calculated by coarse graining Weinhart et al. [2012] all particle data over long simulation time. As this averaged is carried out volumetrically, the reported values are representative of the whole sample and take into account the self-weight of the material. The normal lateral stress σ_{xx} and the shear stress τ_{xy} are approximately uniform across the width of the device, at least for the tested parameters. This represents one of the major advantages of the 3D SSD over the other perpetual shear devices (ring shear and couette) where the stress decays radially.
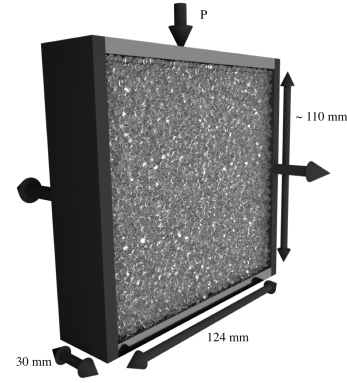

Figure 4. DEM model of a 30 mm slice through the middle of the 3D SSD. The black side panels represent the belt, while the grey panels shows the top and bottom plates; the vertical boundaries with normal in the longitudinal y direction are periodically connected and allow open flow of particles along that direction. The top plate moves to maintain a constant pressure.

Another important observation from the DEM results is contained in Fig. 5(b) with respect to the observed stress ratios. Note that the lateral stresses are approximately the same, as shown by the stress ratio $s \approx 1$. The error bars shown here indicate one standard deviation of these values. While these values are approximately unity for the investigated DEM samples, we expect that the values will increase slightly with increased inter-particle friction and/or inertial number, as reported in Srivastava et al. [2021]. DEM measurements in the stadium shear geometry confirm these observations. For values of $I < 10^{-2}$, increasing the inter-particle friction tends to increase the level of agreement with the assumption of $s \approx 1$.

Since the maximum shear stress must be the one applied by the belt τ_{xy}, it follows that $\sigma_{zz} = \sigma_2$ is the intermediate principle stress, such that Eqs. 8 and 9 hold, and since $s \approx 1$ we find:

$$k_{13} = \frac{1 + \mu}{1 - \mu}, \quad \phi = \arcsin \mu. \quad (13)$$

This latest relation for k_{13} takes the form of Rankine's passive earth pressure coefficient [Rankine, 1857].

Note that this validation is only for steady (critical) state. However, in the following interpretation of the experimental results, we will consider that the $s = 1$ assumption holds true even prior to steady state. In order to validate this assumption prior to steady state, further simulations would be required at various initial densities with significantly larger sample sizes to reduce stress fluctuations in time at early stages of shearing.

3. Experimental methodology

3.1. Calibration procedure

Calibration is carried out to determine the correction coefficient α, the null force F_{N0} and moment $\mathcal{M}_0$ as defined in Eqs. (1,2).
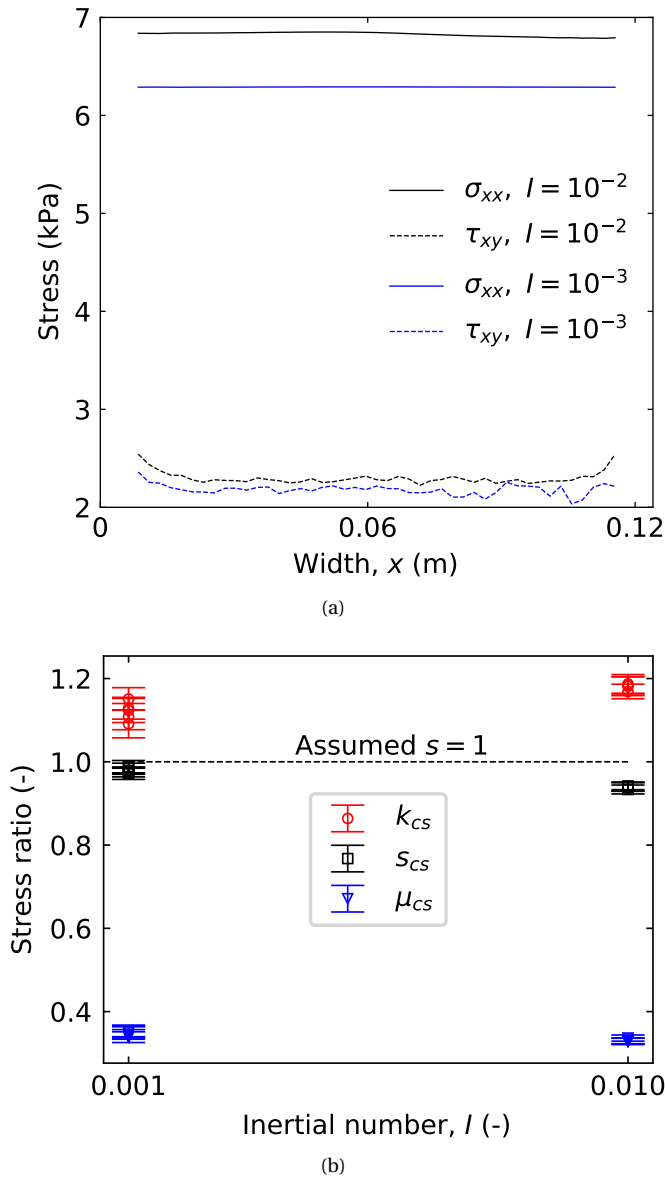
Figure 5. DEM simulation results for: (a) stresses plotted across the width of the sheared system for $I=10^{-3}$ and $I=10^{-2}$ during critical state ; (b) the relation between σ_{xx} and σ_{yy} throughout the entire simulation.

Then the readings from the two load cells and the torque-metre were synchronously recorded while the belt ran at the operating velocity. To avoid any possible creep effects on the measurement instruments, the same measurements were repeated at the end of every experiment, while the readings before and after the tests were averaged. Since the calibration was always made without any material, those measured F_{N0} and $\mathcal{M}_0$ were purely from the mechanical friction mentioned above. Typically, $F_{N0} = 30 \sim 80$ N and $\mathcal{M}_0 = 10 \sim 15$ N.m.

It is important to note that there is significant scope for improvement in both the above calibration procedure and in the design and construction of the device itself to reduce the typical errors that are reported in this paper. For example, the use of lead shot for the calibration of forces could be replaced by developing a more precise approach. Ideally, this procedure would cover the range of stresses to be performed during testing, and would negate any potential arching effects.

As this is the first prototype of the 3D SSD, we have not explored a wide range of designs and construction methods. Some variations in design that could affect the performance of the device are the belt stiffness and homogeneity, alignment of the belt, dimensions of the device, elimination of horizontal loads on the torque meter, and the operational range of load cells and torque meter. In addition, while we have attempted to minimise construction tolerances to eliminate clogging of grains and maintain smooth motion of all components where possible, these factors can all be improved in future versions.

Taking all of these potential issues into account, the experiments reported below provide consistent data of friction coefficients and lateral earth pressure coefficients during granular flow, that compare well with discrete element simulations performed here and elsewhere.

3.2. Samples

The tested samples in this paper include systems of three different glass beads (diameter 1 mm, 3 mm and 14 mm), two different mixtures of Nepean River sand with either uniform or non-uniform particle size distributions and samples of Basalt and Quartz, as pictured in Fig. 6.

The particle density of the glass beads is assumed to be 2400 ± 100 kg/m^3 and their sizes have less than 20% polydispersity. The glass beads are almost spherical, with mean aspect ratio greater than 0.93 (ratio between the smallest and the largest diameter orthogonal to it measured from macrophotographic imaging). In the case of glass beads it is hard to distinguish between the minimum and maximum void ratios; instead, a mean void ratio of 0.645 was found.

The Nepean River sand is a coarse sand normally used as a base compacted material under pavers and retaining walls. The apparent particle density of the Nepean River sand is 2630 kg/m^3 [Aslani and Nejadi, 2013]. Two sand samples with different particle size distributions are prepared from four particle diameter ranges: 0.425 mm ~ 0.6 mm, 0.6 mm ~ 1.18 mm, 1.18 mm ~ 2.36 mm, and 2.36 mm ~ 3.35 mm. One sample, termed G30, comprises of equal weights of

In order to calibrate α, the readings from the two side load cells were compared to a known applied load. Specifically, the device was first tilted horizontally, and then a bag of lead shot with known weight was evenly placed above the side of the belt. This procedure was repeated many times using different weights, and a factor $\alpha = 1.7 \pm 0.1$ was determined to eliminate the differences between the readings of the load cells and the actual weights.

In order to calibrate F_{N0} and $\mathcal{M}_0$, the following procedure was adopted. Before any experiment, when the device had no material inside it, the top plate was first locked at a height close to the one it will have during the experiments.

Open Geomechanics, 2022, article no. 2

Yang Liu, François Guillard, Benjy Marks, Pierre Rognon & Itai Einav, *The perpetual shearing of granular soils under low stresses using the stadium shear device*

7

grains from the four ranges listed above and has a mean diameter D_{50} of 1.2 mm. Another sample, termed G10, only contains grains from the range of diameters 1.18 mm ~ 2.36 mm, and has a D_{50} of 1.7 mm. The particle size distributions for these two sand samples are shown in Fig. 7.

Following the Australian Standard Standards Australia [1998], the maximum void ratio e_{max} of the various sands was obtained by pouring the samples into a mould with a scoop as loosely as possible, while the excess soil level at the top was carefully trimmed off by a straightedge. The minimum void ratio e_{min} was obtained based on the dry method specified in American Society for Testing and Materials [2016] by optimally vibrating (15 minutes including 5 minutes without surcharge and 10 minutes with surcharge) the soil mass at a frequency of 50 Hz under a surcharge of 5 kg while carefully avoiding any grain crushing. The reported e_{max} and e_{min} values are actually averages of repetitive measurements, which showed good repeatability, with differences in void ratios below 0.003. The relevant properties of the various samples are summarised in Table. 1.

To study how the constitutive response depends on the initial packing conditions, initially dense and loose samples were prepared from Nepean River sand G10. The loose sample was prepared by slowly and homogeneously pouring the sand into the device from a minimal distance to the poured free surface. The dense sample was prepared using a different technique, by iteratively compacting sand layers while carefully avoiding the crushing of particles.
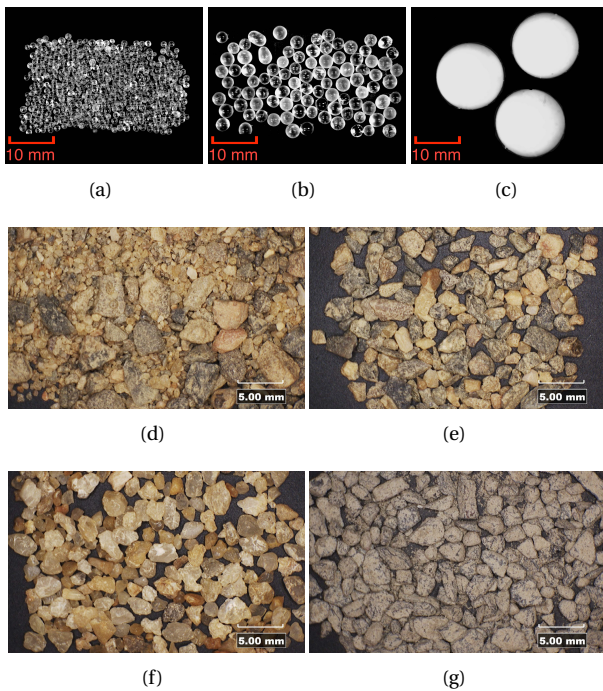
Figure 7. Particle size distributions of the non-uniform (G30) and uniform (G10) Nepean River sand corresponding.

Figure 6. Pictures of the tested granular samples: (a,b,c) 1, 3, and 14 mm diameter glass beads, respectively; (d,e) non-uniform (G30) and uniform (G10) Nepean River sand, respectively; (f) Quartz sand; (g) Basalt sand.
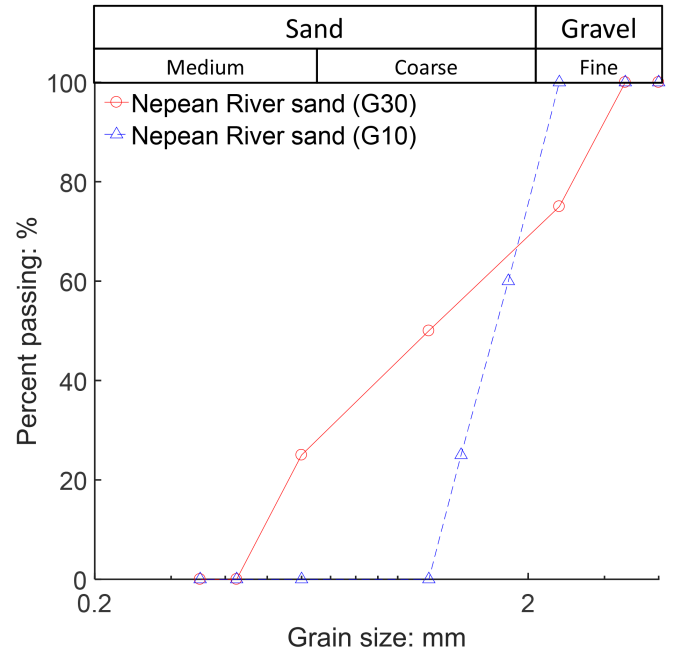
3.3. Experimental campaign — glass beads

A set of tests was conducted with glass beads in order to cross-validate the constitutive response against the DEM model of spherical grains (as shown in Fig. 4). The system was sheared long enough to achieve critical state under a nominal shear rate $\dot{\gamma} = \dfrac{2V_{belt}}{w} \approx 0.114\,\mathrm{s}^{-1}$, where V_{belt} is the belt velocity and w is the width between the two opposite walls of the belt. The 'shear rate' is qualified as 'nominal' to highlight that the shear rate needs not necessarily be uniform throughout the sample, while slip may also potentially develop along the shearing walls of the SSD (although this is assumed to be negligible due to softness of the belt). Nevertheless, in later figures the shear response will be presented in terms of the shear and vertical displacements rather than the shear strain given our current lack of knowledge of potential granular boundary layers (e.g., see Rognon et al. [2015b]) close to the shearing belt. Such kinematic non-uniformities are common in perpetual shear devices, for example in the ring shear device [Toyota et al., 2009]. The confining vertical stress at the centre of the sample, σ_{zz}, is kept constant at 10.6 kPa during the test. This stress is predetermined and comprises contributions from: (1) the added weights; (2) the self-weights of the top plate and loading frame; (3) the self-weight of half of the sample's height. This stress is low enough to avoid either grain crushing or sintering. Stress data were smoothed with a moving window over 80 s. Thanks to the measurements of the normal lateral stress σ_{xx} and shear stress τ_{xy} on the long sides of the belt, the evolution of the friction coefficient μ and stress ratio k (defined in Eqs. 3) can be tracked over the entire shear duration.

Table 1. Sample properties.

Sample	Mean diameter D_{50} (mm)	Density (kg/m^3)	Gravel content (%)	e_{max} -	e_{min} -
Glass beads	1, 3, 14	2400±100	-	-	-
Nepean River sand (G30)	1.5	2630	30	0.75	0.47
Nepean River sand (G10)	1.7	2630	10	1.01	0.66
Basalt	1.6	2750	10	1.18	0.85
Quartz	1.6	2650	10	0.96	0.59

A variety of tests with different glass beads were conducted over a wide range of inertial numbers I (see definition in Eq. 12) from 10^{-6} to 10^{-2} to study possible rate effects of the friction coefficient μ, as widely studied in granular physics [Bagnold, 1954, Bouzid et al., 2013, da Cruz et al., 2005, Hatano, 2007, Jop et al., 2006, Koval et al., 2009, Peyneau and Roux, 2008] and geophysics [Bridgewater, 1972, Hanes and Inman, 1985, Hungr and Morgenstern, 1984, Morrow and Byerlee, 1989, Omidvar et al., 2012, Tika and Hutchinson, 1999, Tika et al., 1996]. Here, the focus is on confirming the usual geotechnical assumption of rate independence under slow rates (low I, typically under 10^{-2}). To achieve these relatively small inertial numbers the glass bead systems were sheared under nominal shear rates from 0.0114 to 1.14 s^{-1} at a constant vertical confining stress of 10.6 kPa. The shear and normal stresses were first measured under the lowest shear rate, and incrementally increased the shear rate to the highest possible. High reproducibility was indicated by repeating the same test from the highest shear rate to the lowest. Further discussion about the critical state is addressed in the Results and Discussions section.

3.4. Experimental campaign — Natural sand

The SSD was further employed to carry out perpetual shear tests with Nepean River sand. To study the effect of the initial density, the material was prepared into four distinct initial densities ranging roughly from the minimum to the maximum void ratios, using similar techniques to those mentioned earlier. Shear tests were conducted under nominal shear rates ranging from $\dot{\gamma}$ = 0.0114 to 1.14 s^{-1} and low confining stresses to limit abrasion, 4.6 kPa, until the system reached steady state and then continuously sheared along the critical state. Stress data were smoothed with a moving window over 80 s, so that the stress coefficients can be tracked. In addition, the dilatancy potential of the samples was investigated. Tests with the two other natural sands, Basalt and Quartz, were carried out to examine the role of particle morphology on the measured friction angle and lateral stress ratio values.

4. Results and discussions

4.1. Cross-validation with glass beads

The purpose of this Section is to address the assumptions stated in point (3) of Section 2.4 that the roughness of the top and bottom boundaries does not affect the measured behaviour, as well as cross-validating the DEM and the experiments in the case of spheres/glass beads. For the case of the sheared 3 mm glass beads system under constant vertical normal confining stress of 10.6 kPa, the friction coefficient μ and stress ratio k are shown in Fig. 8 for both the DEM and experiments. The value of μ stays at a relatively constant value of approximately 0.31, with small fluctuations (approximately 15%), while the stress ratio k peaks at a value of approximately 1.05 during the first 1000 s and then decreases and stabilises at around 1.03 for the remaining deformation. Both coefficients reach a stable value after approximately 5000 mm shear displacement, which corresponds to critical state. Considering the nominal homogeneous shear rate of 0.114 s^{-1}, this shear time corresponds to a substantial nominal strain of $\approx$ 570, far and beyond conventional shear devices.
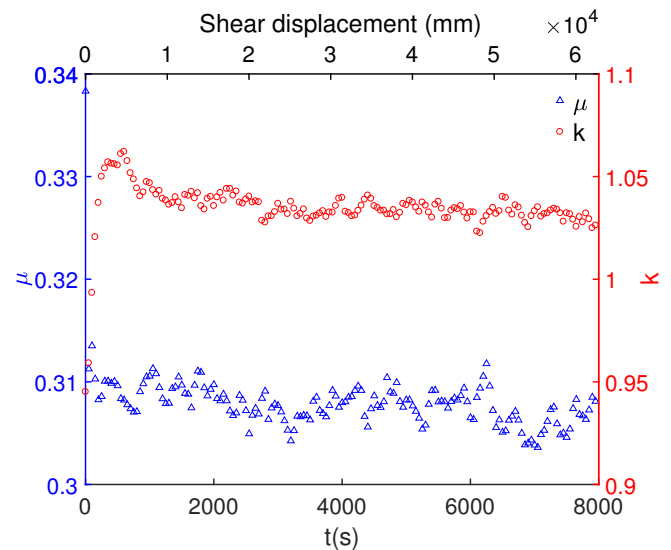

Figure 8. The friction coefficient μ and stress ratio k for the case of the sheared 3 mm glass beads system, with normal confining stress of 10.6 kPa and shear rate of 0.114 s^{-1}.

By conducting additional experiments using 1 mm and 14 mm glass beads at different shear rates, it is possible to establish that the critical state friction coefficient μ_{cs} does not change as a function of inertial number I for the range $10^{-6} \sim 10^{-2}$ (see Fig. 9(a)). The data in Fig. 9(a) represents the average of μ recorded beyond 5000 mm shear displacement, during the critical state, with error bars of one standard deviation. Note that the error bars for the 14 mm glass beads are larger than those for the smaller beads due to the substantially smaller number of grains in contact with the belt at any given time, which therefore causes the force to fluctuate more pronouncedly. Also note that to calculate the

Open Geomechanics, 2022, article no. 2

Yang Liu, François Guillard, Benjy Marks, Pierre Rognon & Itai Einav, *The perpetual shearing of granular soils under low stresses using the stadium shear device*   9

inertial number, the value of $s = 1$ was adopted ($\sigma_{xx} = \sigma_{yy}$), as shown to be valid during the DEM simulations (see Fig. 5).

Note that the data sets for μ and k corresponding to when the shear rate is either gradually incremented upwards or gradually incremented downwards are notably similar. This proves that both the particles and the apparatus did not experience any gradual permanent alternation to their shapes. This conclusion is reinforced by the fact that grain crushing was not observed during the tests, as one would expect under relatively low stresses.

Quantitatively, in all the tests we find that the value of μ during large strains fluctuates only slightly around a critical state value of μ_{cs} between 0.31 ~ 0.38 without showing any clear shear rate dependency. This shear rate independence in the quasi-static regime is in agreement with previous studies [Da Cruz et al., 2002, 2003, Iordanoff and Khonsari, 2004]. Moreover, the value of μ_{cs} from our experiments agrees both qualitatively and quantitatively with the $\mu(I)$ rheology relationship [Jop et al., 2005], where the friction coefficient μ tends to a minimum value μ_0 at low $I \lesssim 0.1$, and μ_0 is found to be equal to 0.38 for glass beads [Forterre and Pouliquen, 2003], which is close to our measured value. Note that for our glass beads we do not find the weak negative dependence of the friction coefficient μ under $I < 10^{-3}$ observed in sand by Hatano [2007]. Although the current configuration was designed for low shear rates, based on the $\mu(I)$ relationship we might expect to find rate dependence for situations with $I > 10^{-2}$. Future modifications are currently planned to be implemented in order to increase the range of accessible inertial numbers, and to confirm the expected rate dependence. The normal stress ratio k shows a similar shear rate independence in Fig. 9(b), but a clear grain size effect is visible in that case, i.e. k increases with increasing grain size.

The resultant stress ratios μ and k are plotted in Fig. 9(a) and Fig. 9(b) for three values of the grains to plates sliding coefficient $\mu_s = 0$, 0.15 and 0.3, respectively. It indicated that there was no obvious dependence of μ_s on both stress ratios. The results are also included in Fig. 9(a) and Fig. 9(b). In comparison with the experimental data, the DEM results generally show an excellent agreement except that the k values are slightly higher in simulations than in the corresponding experimental measurements. Note that the k_{cs} values from both the DEM and experiments consistently increase with increasing grain size, which may be explained by grain frustration in confined geometries [Marks et al., 2015]. Experimental data for 3 mm glass beads at higher values of $I > 10^{-2}$ is lacking due to the limitations of the current set-up of the device.

Finally, note that the resultant stress ratios μ and k from our DEM model simulations are also reported in Fig. 9(a) and Fig. 9(b) for different shear rates and friction coefficients between the grains and the loading plate. The values reported from the DEM are taken from forces applied only at the boundaries of the system, which are smaller than the experimental boundaries due to the periodic boundary conditions used. In comparison with the experimental data, the DEM results generally show an excellent agreement except that the k values are slightly higher. This confirms the
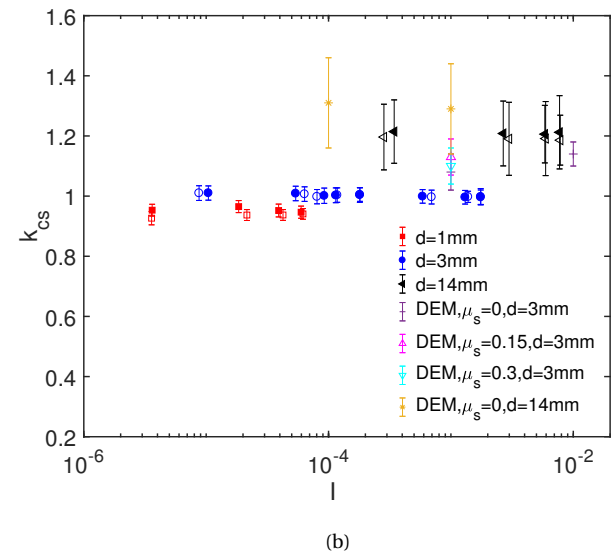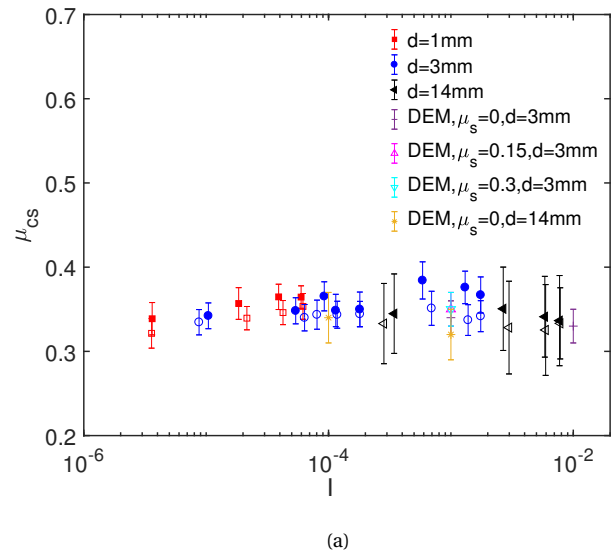

(a)

(b)

Figure 9. Shear rate dependence of stress ratios (a) μ_{cs} (μ at critical state) (b) k_{cs} (k at critical state) for glass beads, with normal confining stress of 10.6 kPa. The filled makers indicated the results when shearing the sample from the lowest to the highest velocity, and the unfilled makers showed the results when shearing the sample from the highest to the lowest velocity. Error bars indicate one standard deviation of the measured values along the boundaries.

accuracy of the stress measurements in the SSD, and proves the minimal effect of the friction along the upper and lower boundaries. Overall, no shear rate dependence is observed over the range $10^{-6} < I < 10^{-2}$, and similarly there is no observed dependence on incrementing or decrementing the shear rate between experiments, confirming the absence of modification of either the sample or the apparatus during the experimental campaign.

Open Geomechanics, 2022, article no. 2
Yang Liu, François Guillard, Benjy Marks, Pierre Rognon & Itai Einav, *The perpetual shearing of granular soils under low stresses using the stadium shear device*

10

4.2. Natural sand — the influence of initial relative density

After validating the SSD by shearing samples of glass beads and comparing with DEM simulations, in this section the behaviour of a natural sand (Nepean River sand G10) is analysed in terms of the shear strength and dilatancy potentials in samples with four different initial void ratios e from 0.74 to 0.91. Fig. 10(a) shows the vertical versus shear displacements for the different initial void ratios tests, with the vertical displacements being measured using an LVDT, where positive values indicate sample dilation, and negative values indicate compaction. At the onset of shearing, the vertical displacement always begins with a short compaction phase, but then the samples significantly dilate over much larger shear displacements. The initially densest sample experienced the largest dilation with about 15 mm upwards plate displacement, while the initially loosest sample underwent the smallest dilation. Similar observations were made by Fannin et al. [2005] using direct shear box tests on cohesionless soils under low stresses.

To further examine the dilatancy behaviour of Nepean River sand under low stresses, Fig. 10(b) shows the evolution of the relative density $Dr = (e_{max} - e)/(e_{max} - e_{min})$ during shearing under a nominal shear rate of $0.0114 \, s^{-1}$ and a vertical confining pressure of 4.6 kPa. Curves start from different initial Dr and in all tests performed in this paper exhibit dilatancy behaviour, which begins only after a small amount of initial compaction at the beginning of shear (from the onset of shear to roughly 50 mm shear displacement). When samples dilate they do so at different rates, and eventually reach a terminal $Dr = 0$ after more than 1500 mm shear displacement. Considering a shear thickness of ≈ 124 mm, this displacement corresponds to a substantial nominal strain of ≈ 12, far and beyond conventional shear devices. From this point onwards the sample is at critical state, with critical state void ratio independent of the initial void ratio [Schofield and Wroth, 1968, Wood, 1990]. The critical state value of $Dr = 0$ is expected under such low stress conditions and no grain crushing [Tengattini et al., 2016].

As shown in Fig. 11, the dilatancy potential can be compared using the slope of the displacement curves of Fig. 10(a). Specifically, Fig. 11 shows the ratio between the instantaneous volumetric change ΔV over the shear deformation change ΔS. Since the lateral deformation in both the x and y directions are practically zero due to the rigidity of the belt and the two confining plates located on its sides (Fig. 1(b)), the volumetric change ΔV is equal to the vertical displacement. The maximum dilatancy potential corresponds to the peak of the curves developing after about 50 mm shear displacement. After more than about 500 mm shear displacement all the tests were essentially sheared at constant volume ($\Delta V/\Delta S = 0$), regardless of the initial density, which is again a sign of critical state conditions. The significant dilatancy exhibited was expected since the tests were conducted under low vertical confining stresses, which allowed for compliant changes to the sample height. Similar observations of initial contraction before significant
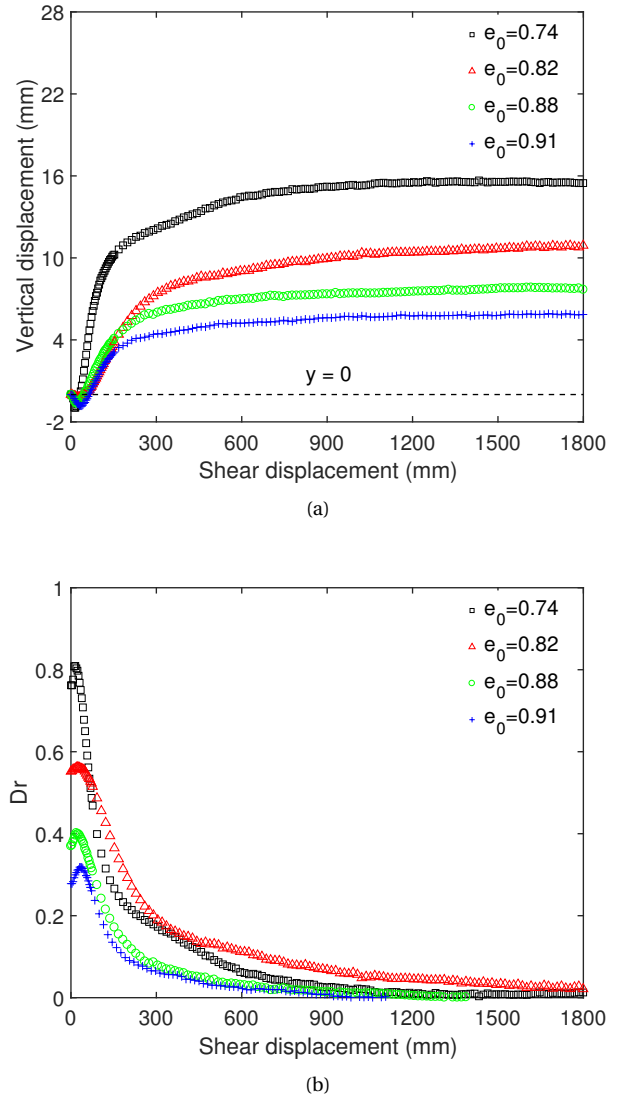

(a)

(b)

Figure 10. The evolution of: (a) the vertical displacement and (b) the relative density Dr of sheared Nepean River sand under constant $\sigma_{zz} = 4.6$ kPa at a constant shear rate of $0.0114 \, s^{-1}$.

dilation was reported by Fannin et al. [2005] using direct shear box tests on cohesionless soil at low stress.

The inset of Fig. 11 shows the maximum dilatancy potential as a function of the relative density, and reveals a clear positive correlation indicated by the linear fitting line. In other words, samples with higher initial relative density dilate faster, but the peak dilatancy potential is attained after roughly the same amount of shear displacement irrespective of the initial density. Similar correlations have been found by Bolton [1986] and later by Chakraborty and Salgado [2010] based on the examination of a large number of plane-strain and triaxial tests from low (4 kPa) to high confining stresses (600 kPa).

The shear stress τ_{xy} and normal stress σ_{xx} during these different initial density tests are shown in Fig. 12. All curves

Open Geomechanics, 2022, article no. 2
Yang Liu, François Guillard, Benjy Marks, Pierre Rognon & Itai Einav, *The perpetual shearing of granular soils under low stresses using the stadium shear device*
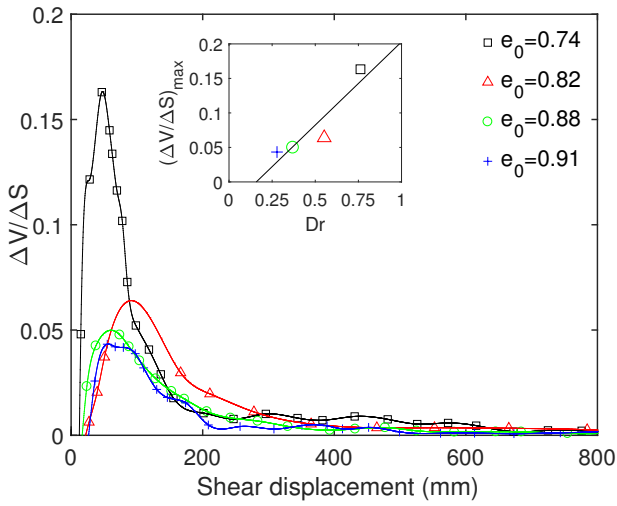
11

Figure 11. Dilatancy potential (ratio between changes in vertical displacement over changes in shear displacement) for four different initial density tests of the Nepean River sand, under constant confining stress σ_{zz}=4.6 kPa and shear rate of 0.0114 s^{-1}. Inset shows the maximum dilatancy potential versus the initial relative density.
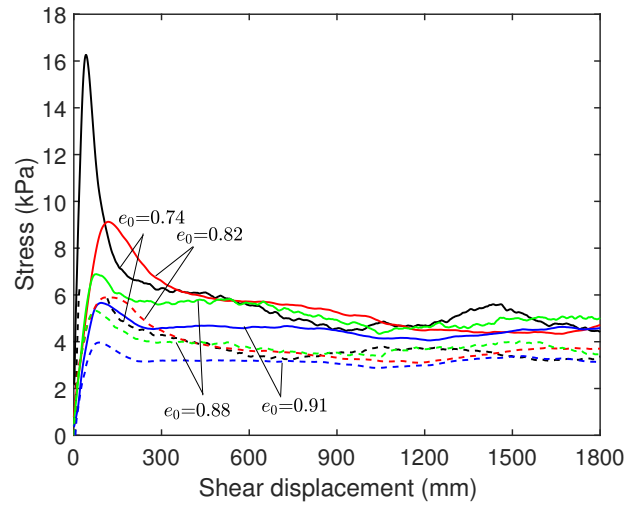

Figure 12. The normal and shear stresses measured from the shear tests on four different initial packing systems of Nepean River sand over a total of 1800 mm of shear displacement at a shear rate of 0.0114 s^{-1}, under 4.6 kPa normal confining stress. Solid lines represent the normal stress and dashed lines indicate the shear stress. (Note that some of the shear stress data for the e_0=0.74 test are not shown, as the torque transducer reached its upper limit.)

peak at a shear displacement similar to the one corresponding to the maximum dilatancy potential in Fig. 11, which is consistent with [Bolton, 1986], before they soften gradually to their critical state values after about 600 mm shear displacement.

Stress development during the tests is further investigated in terms of the dimensionless stress ratios μ and k in Fig. 13(a) and Fig. 13(b), respectively. The maximum peak value of μ for all the curves is approximately 1.17; such a μ gives a maximum peak friction angle of 49.5° (using Eq. 13). An ultimate value of $\mu \approx 0.69$ is common to all of the tests and corresponds to a critical state friction angle of ϕ_{cs}=43.6°.
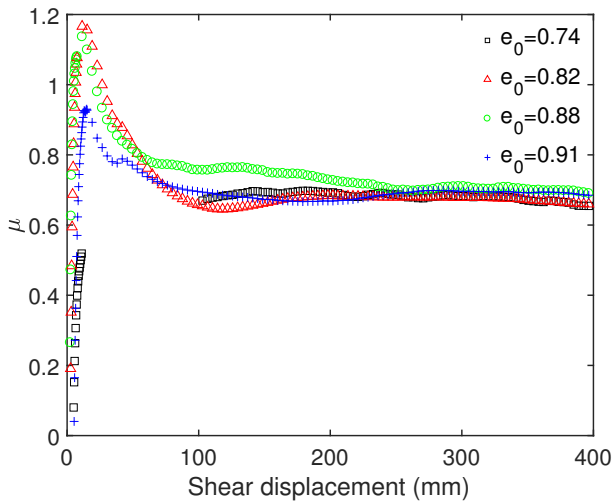
The evolution of k during shear follows the same trend as the normal stress curves plotted in Fig. 12 simply because k is defined as the ratio of σ_{xx} and σ_{zz}, while σ_{zz} is constant. One can find that the critical state value of k is $k_{cs} \approx 1$.

Fig. 14(a) and Fig. 14(b) show how μ and k develop as a function of the relative density Dr during shear, for different initial Dr conditions. One obvious result is that μ increases to its peak value without significant change to the relative density Dr, irrespective of the initial value of Dr (approximately vertical lines in Fig. 14(a)). Shortly after the peak value of μ, the relative densities Dr slightly increase by an amount that decreases for the higher initial Dr tests, in a manner that is directly related to the commonly observed phenomenon where samples slightly contract before dilating during shear [Fannin et al., 2005, Rowe, 1962, Tatsuoka et al., 1986]. The ultimate value of μ, $\mu_{cs} \approx 0.69$, is independent of the initial Dr, confirming the attainment of critical state. As can be seen in Fig. 14(b), k increases from a near-zero
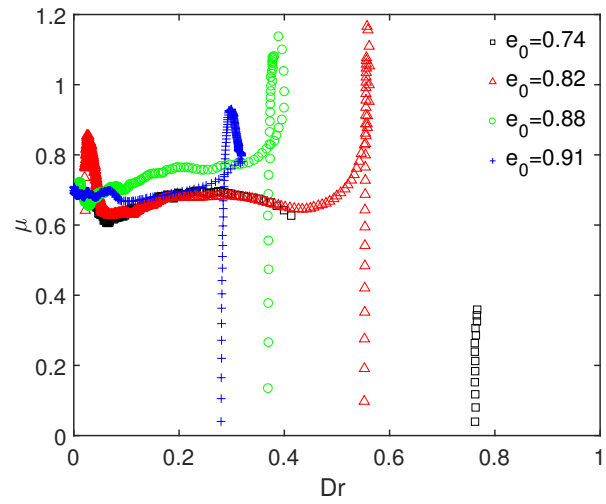
value towards a peak value, before reducing towards an ultimate, critical state value of $k_{cs} \approx 1$ during which all samples dilated towards Dr = 0. In other words, given the assumption $s = 1$ it is found that under critical state all the normal stresses are equal in the cartesian frame of reference of the SSD ($\sigma_{xx} = \sigma_{yy} = \sigma_{zz}$). In the absence of shear stresses this would correspond to the case of classical fluids; but here, of course the shear stresses at critical state are non-zero, as expected from frictional materials. The dependence of the peak and critical state values of $\phi = \tan^{-1} \mu$ and k on the initial relative density $Dr_0 = (e_{max} - e_0)/(e_{max} - e_{min})$ is shown in Fig. 15. The peak values generally grow with Dr_0, whereas the critical state values are relatively constant.

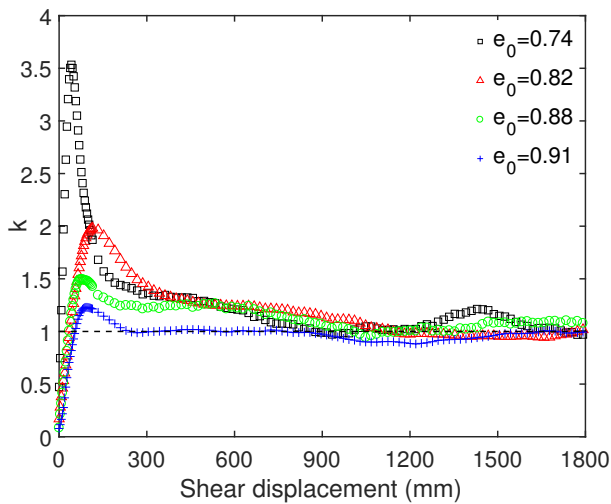## 4.3. Natural sand — the influence of particle size distribution

For Nepean River sand, the effect of the particle size distribution on the rate dependence of the critical state values of $\mu = \mu_{cs}$ and $k = k_{cs}$ are shown in Figs. 16(a) and 16(b), respectively. Unlike the case of glass beads, over a similar range of inertial numbers, we find μ_{cs} has an apparent positive shear rate dependence for both the G30 and G10 samples. However, k_{cs} is independent of the rate and remains fairly constant and slightly higher for the more well graded sample G30 (of 30% gravel content). Moreover, the value of μ_{cs} for the more well graded sample G30 was higher than that of the poorly graded sample G10 (10% gravel content) under all shear rates; in other words, the shear strength is found to increase with grain size polydispersity. Simoni and Houlsby [2006] drew a similar conclusion using
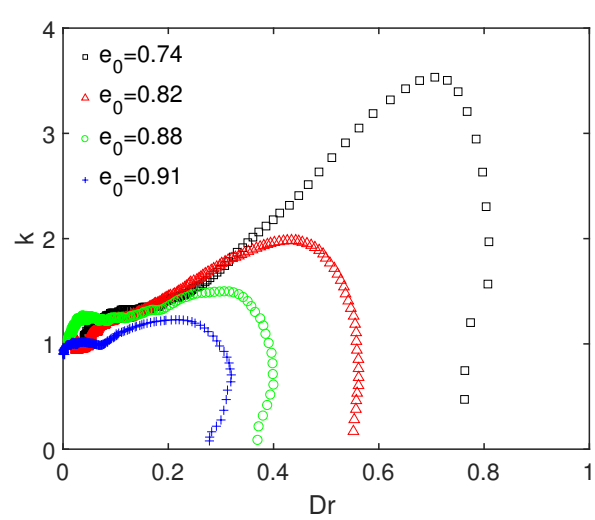
Open Geomechanics, 2022, article no. 2
Yang Liu, François Guillard, Benjy Marks, Pierre Rognon & Itai Einav, *The perpetual shearing of granular soils under low stresses using the stadium shear device*

12

(a)

(b)

Figure 13. The stress ratios (a) μ and (b) k plotted against shear displacement at σ_{zz}=4.6 kPa and a shear rate of $0.0114\,\mathrm{s}^{-1}$. (Notice that some of the μ data for the e_0=0.74 test are not shown, as the torque transducer reached its upper limit.)

(a)

(b)

Figure 14. The stress ratios (a) μ and (b) k plotted against relative density Dr at σ_{zz}=4.6 kPa and shear rate of $0.0114\,s^{-1}$. (Note that some of the μ data for the e_0=0.74 test are not shown, as the torque transducer reached its upper limit.)

direct shear tests with different mixtures of sand and gravel (though without exploring the effect of the shear rate).

Nevertheless, it should be noted that DEM-based numerical results seem to often suggest that the shear strength is independent of the grain size distribution. While such DEM simulations always involve model idealisations, which raise questions on the validity of the adopted contact laws at the presence of high contact number in polydisperse samples, especially for large particles, DEM studies can enable to decouple grain shape from size effects. On the contrary, this is not the case in natural sand where particle size and shape are normally intertwined, and so the increase of friction with
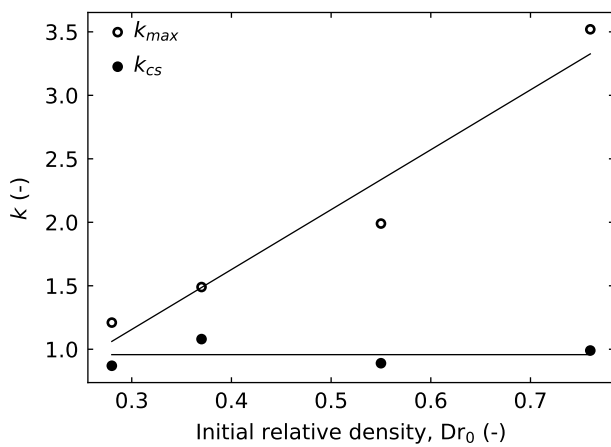
polydispersity might actually arise directly due to this coupling.

4.4. Natural sand — the influence of particle shape

Here we employ the 3D SSD to demonstrate the role of particle shape on the shear strength and dilatancy of granular soils at low vertical confining stresses. Three samples, Quartz, Nepean River Sand (G10) and Basalt were sheared to
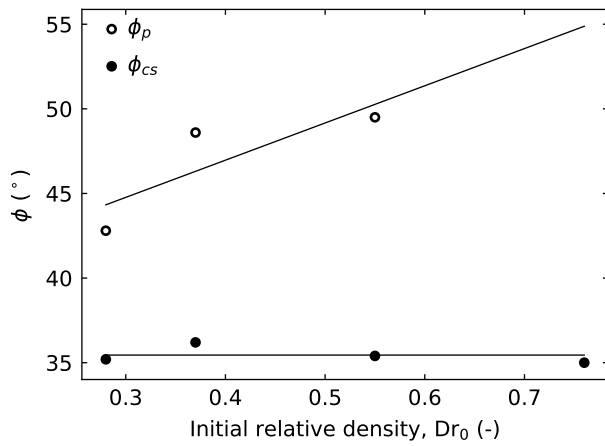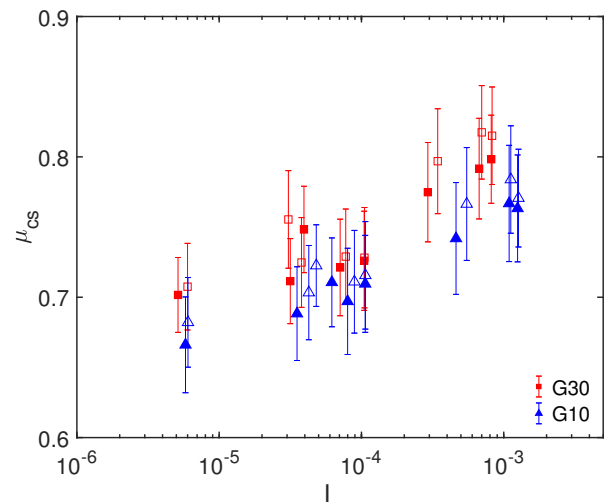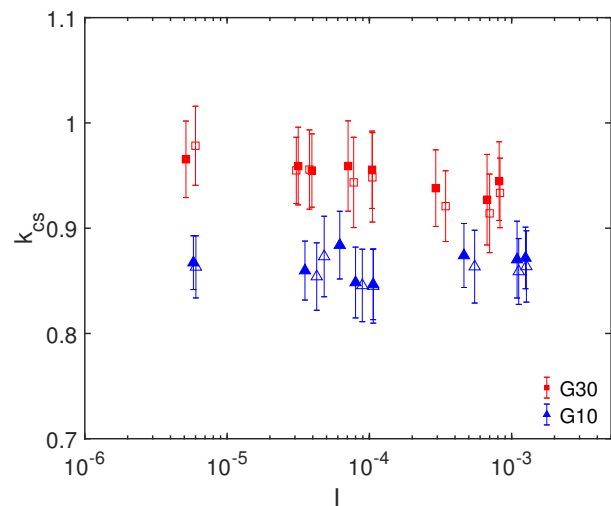
(a)

(b)

Figure 15. The effect of initial relative density on the peak and critical state friction angle and lateral stress ratio. Solid lines for the peak values indicate a linear best fit, while for the critical state indicate the average. The value of ϕ_p for the largest Dr_0 was not measured as described in the text.

(a)

(b)

Figure 16. The effect of particle size distribution on the shear rate dependence of stress ratios (a) μ_{cs} (at critical state) and (b) k_{cs} (at critical state) for Nepean River sand, with normal confining stress at 7.6 kPa. G30 represents samples with 30% gravel content, while G10 samples with 10% gravel content. Filled makers indicate results where the belt velocity was incremented from the lowest to the highest velocity, whilst unfilled makers show results from decrementing the velocity.

a large deformation at a shear rate of 0.0129 s^{-1} and a vertical confining stress of 1.5 kPa. Samples with the same particle diameter were prepared to comparable initial relative densities, to eliminate the effect caused by the initial density of the results.

Table 2 summarises the particle shape properties of three natural sands: Quartz, Nepean River sand, and Basalt. The properties are obtained from testing samples with a Morphologi G3 device which provides the ability to measure the morphological characteristics (size and shape) of particles. The morphology device can measure a variety of shape factors, including circularity, convexity and roundness. Circularity ($\frac{4\pi A}{P^2}$, where A is the particle area and P is its perimeter) is a factor to quantify how close the shape is to a perfect circle. A perfect circle has a circularity of 1 while a 'spiky'

or irregular object has a circularity value closer to 0. Convexity is another measure of shape calculated by dividing the convex hull perimeter by the actual particle perimeter. A smooth shape has a convexity of 1 while a 'spiky' or irregular object has a convexity close to 0. Roundness ($\frac{4A}{\pi x^2}$, where x is the length of the major axis of the particle in the imaging plane), like circularity, measures how close the shape of a

Open Geomechanics, 2022, article no. 2

Yang Liu, François Guillard, Benjy Marks, Pierre Rognon & Itai Einav, *The perpetual shearing of granular soils under low stresses using the stadium shear device*

14

Table 2. Particle shape properties and particle images of different natural samples. Things that are constant: sieved between 1.18 and 2.36 mm. Initial relative density around 0.58. Vertical stress 1.5 kPa. Shear strain rate 0.0129 s^{-1}.

Sample	Circularity	Convexity	Roundness	Sample image
Quartz	0.78	0.95	0.83	
Nepean River Sand (G10)	0.66	0.91	0.69	
Basalt	0.54	0.81	0.56	
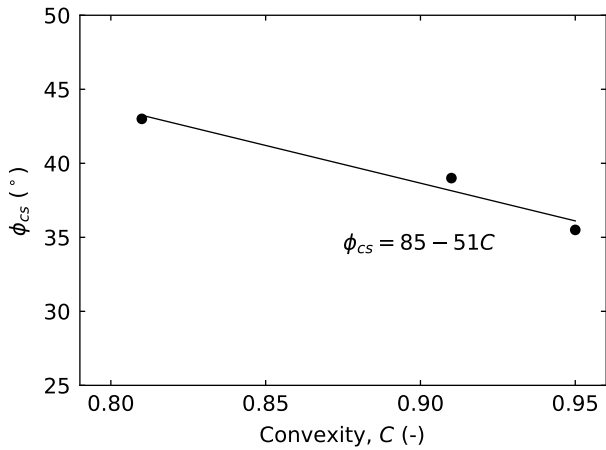
(a)
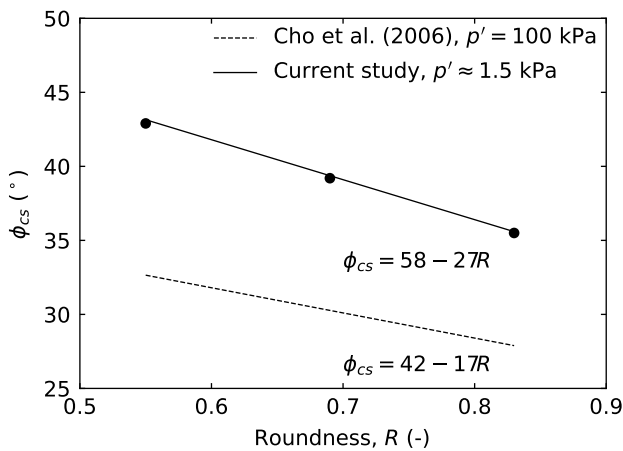
(b)

Figure 17. The effect of particle convexity and roundness on the critical state friction angle. Solid lines indicate a linear best fit.

particle approaches that of a perfect circle. Quartz particles have the highest circularity, roundness and convexity, while Basalt has the largest angularity.

We observe in Fig. 17 that the critical state friction angle at low confining stress decreases with both convexity and roundness. Similar results have been found in [Cho et al., 2006] for a wide range of material and a much higher confining pressure. The decrease of friction angle with stress, especially at low stress, has been reported previously [Rousé, 2018] from direct shear box testing.

4.5. Potential finite size effects in the SSD geometry

Like any other apparatus, the SSD involves boundaries and contains a finite volume. Here we discuss the conditions by which the dimensions associated with this finite volume may affect the observed material behaviour.

First, granular materials are known to exhibit non-local effects which develop in the presence of stress gradients Kamrin and Koval [2012] or near walls Miller et al. [2013], Rognon et al. [2015b]. The plane shear geometry of the SSD has been specifically designed to eliminate stress gradients as much as possible – between two parallel boundaries, the continuity equation for momentum predicts that both the shear and normal stresses are homogeneous. Nonetheless, the effective viscosity of the material does tend to decrease near walls Miller et al. [2013], Rognon et al. [2015b]. While this means that the shear rate profile might not be constant, the effect of this on the effective friction coefficient in a 2D SSD configuration was found to be negligible when the gap (between the two sides of the belt) is greater than 20 grain size Rognon et al. [2015b]. As a comparison, the narrowest gap considered here is 37 grains of size 3.35 mm. Nonetheless, based on Miller et al. [2013], Rognon et al. [2015b] it is expected that narrow gaps or larger grains could produce significant finite size effect on the measured friction law.

Second, the assumption of homogeneous stresses between the moving walls (the belt) may not be valid for any gap size. The mobilised friction between the material and the top and bottom plates may introduce some stress heterogeneity. In the limit of a very large gap, this friction may screen the shear and normal stresses in the x direction. Stresses would expectantly be maximal near the belt and lower in the centre. In the limit of a very narrow gap, the vertical friction developing between the flowing material and the belt could induce a "Janssen effect", by which the vertical normal stress imposed on the top plate vanishes within the material. Having an aspect ratio between the gap width and height of the order of one is a natural choice to avoid both of these limits.

5. Conclusions

A new soil testing device (the stadium shear device, SSD) was developed and employed, with a focus devoted to the engineering behaviour of granular soils under low stresses. One of the advantages of the SSD device is its ability to impose perpetual shear (*i.e.*, arbitrarily large shear deformation). The stress conditions developed during shear were studied with the help of Discrete Element Method (DEM) simulations. In particular, the DEM simulations replicated the physical shearing of glass beads systems with the SSD, and accurately captured the measured stresses during the physical tests. The DEM model also demonstrated that the stresses across the tested samples are practically uniform, another major advantage of using the SSD. The significance of this stress uniformity in the SSD should be highlighted, especially since the stresses in the previous perpetual shear devices of granular soils (the ring shear and couette flow devices) are not uniform and decay radially. Moreover, for spherical particles, the discrete numerical simulation showed that the normal stresses in the horizontal planes are essentially equal.

With this information, it was possible to determine the full stress state of the material under perpetual shear, *ie.*, to find the four non-zero stress components: the vertically imposed stress, the measured and evaluated lateral stresses, and the imposed shear stress. Using these four stresses, three dimensionless stress ratios were defined (the friction coefficient μ, and two normal stresses ratios, k and s, the latter being shown to be approximately equal to unity from the DEM simulations). The friction coefficient μ was first explored for the glass beads systems, which demonstrated no shear rate dependence for the range of tested shear rates. Conversely, the friction coefficient μ of sub-angular particles (Nepean River sand) increased with increasing shear rates and particle size polydispersity. The stress ratio k between the lateral normal stress and vertical normal also showed rate independence with values close to unity for both the round (glass beads) and sub-angular (sand) particles.

Under the low stresses applied (under 10 kPa), the sand also showed dilation, with the dilatancy potential being affected by the initial packing condition. While the maximum dilatancy potential of the different tests was linearly correlated with the initial relative density, samples starting from denser initial packings exhibited higher dilatancy potential. However, as tests progressed to their ultimate critical state (a state that cannot be truly reached using standard testing devices such as the triaxial shear cells and shear boxes), the sand density always progressed to its lowest relative density (maximum void ratio), regardless of its initial packing condition.

The SSD already provides a measure of the stress state of soil in a controlled way, allowing infinite shear of the material and constant stress across the cell. The very slow relaxation of the stress towards critical state under substantially large deformations, for example as shown in Figs. 13(a) and 13(b), corroborates the usefulness of the SSD for deriving the true critical state properties of sheared granular soils. Future developments and analysis are required to be undertaken in order to broaden the scope of the device. Given that the material in the SSD studied in the present paper was confined in the lateral direction, the corresponding normal lateral strains were essentially zero. Additionally, the vertical strain was measured, as well as the nominal shear strain. However, future research is needed in order to evaluate the exact kinematics developing within the device. These kinematics may involve boundary layers that could potentially develop along the belt (e.g., as demonstrated through 2D SSD investigations [Miller et al., 2013, Rognon et al., 2015a,b]); this could be studied using an X-ray transparent SSD where grain motions can be analysed using the X-ray facility for fast granular flows at the University blinded[Baker et al., 2018, Guillard et al., 2017]. Moreover, extension of the SSD for larger stresses and higher velocities should also be implemented.

Conflicts of Interest

The authors declare no conflicts of interest. The complete review history is available online.

Acknowledgements

References

Allersma, H. G. (1987). *Optical analysis of stress and strain in photoelastic particle assemblies.* PhD thesis, Delft University of Technology, The Netherlands.

American Society for Testing and Materials (2016). Standard testing methods for maximum index density and unit weight of soils using a vibratory table. Standard, PA: American Society for Testing and Materials, Philadelphia.

Aslani, F. and Nejadi, S. (2013). Self-compacting concrete incorporating steel and polypropylene fibers: Compressive and tensile strengths, moduli of elasticity and rupture, compressive stress–strain curve, and energy dissipated under compression. *Composites Part B: Engineering*, 53:121–133.

Bagnold, R. A. (1954). Experiments on a gravity-free dispersion of large solid spheres in a newtonian fluid under shear. *Proceedings of the Royal Society of London. Series A, Mathematical and Physical Sciences*, 225(1160):49–63.

Baker, J., Guillard, F., Marks, B., and Einav, I. (2018). X-ray rheography uncovers planar granular flows despite non-planar walls. *Nature communications*, 9(1):1–9.

Bandini, V. and Coop, M. R. (2011). The influence of particle breakage on the location of the critical state line of sands. *Soils and Foundations*, 51(4):591–600.

Bishop, A. W., Green, G., Garga, V. K., Andresen, A., and Brown, J. (1971). A new ring shear apparatus and its application to the measurement of residual strength. *Géotechnique*, 21(4):273–328.

Open Geomechanics, 2022, article no. 2
Yang Liu, François Guillard, Benjy Marks, Pierre Rognon & Itai Einav, *The perpetual shearing of granular soils under low stresses using the stadium shear device*

16

Bocquet, L., Losert, W., Schalk, D., Lubensky, T., and Gollub, J. (2001). Granular shear flow dynamics and forces: Experiment and continuum theory. *Physical Review E*, 65(1):011307.

Bolton, M. (1986). The strength and dilatancy of sands. *Géotechnique*, 36(1):65–78.

Bosdet, B. W. (1980). *The UBC ring shear device*. PhD thesis, University of British Columbia.

Bouzid, M., Trulsson, M., Claudin, P., Clément, E., and Andreotti, B. (2013). Nonlocal rheology of granular flows across yield conditions. *Physical Review Letters*, 111(23):238301.

Bridgewater, J. (1972). Stress-velocity relationships for particulate solids. In *Mechanical Engineering*, page 60, New York. American Society of Mechanical Engineering, New York, NY 10017.

Carrier, W. D., Olhoeft, G. R., and Mendell, W. (1991). Physical properties of the lunar surface. *Lunar Sourcebook*, pages 475–594.

Chakraborty, T. and Salgado, R. (2010). Dilatancy and shear strength of sand at low confining pressures. *Journal of Geotechnical and Geoenvironmental Engineering*, 136(3):527–532.

Chambon, G., Schmittbuhl, J., Corfdir, A., Vilotte, J., and Roux, S. (2003). Shear with comminution of a granular material: Microscopic deformations outside the shear band. *Physical Review E*, 68(1):011304.

Cheng, X., Lechman, J. B., Fernandez-Barbero, A., Grest, G. S., Jaeger, H. M., Karczmar, G. S., Möbius, M. E., and Nagel, S. R. (2006). Three-dimensional shear in granular flow. *Physical Review Letters*, 96(3):038001.

Cho, G.-C., Dodds, J., and Santamarina, J. C. (2006). Particle shape effects on packing density, stiffness, and strength: natural and crushed sands. *Journal of Geotechnical and Geoenvironmental Engineering*, 132(5):591–602.

Da Cruz, F., Chevoir, F., Bonn, D., and Coussot, P. (2002). Viscosity bifurcation in granular materials, foams, and emulsions. *Physical Review E*, 66(5):051305.

Da Cruz, F., Chevoir, F., Roux, J., and Iordanoff, I. (2003). Macroscopic friction of dry granular materials. *Tribology Series*, 43:53–61.

da Cruz, F., Emam, S., Prochnow, M., Roux, J.-N., and Chevoir, F. (2005). Rheophysics of dense granular materials: Discrete simulation of plane shear flows. *Physical Review E*, 72(2):021309.

Einav, I., Rognon, P., and Miller, T. (2014). Device for determining material properties. US Patent 8,701,498.

Fannin, R., Eliadorani, A., and Wilkinson, J. (2005). Shear strength of cohesionless soils at low stress. *Géotechnique*, 55(6):467–478.

Fenistein, D., van de Meent, J. W., and van Hecke, M. (2004). Universal and wide shear zones in granular bulk flow. *Physical Review Letters*, 92(9):094301.

Forterre, Y. and Pouliquen, O. (2003). Long-surface-wave instability in dense granular flows. *Journal of Fluid Mechanics*, 486:21–50.

Fuchs, R., Weinhart, T., Meyer, J., Zhuang, H., Staedler, T., Jiang, X., and Luding, S. (2014). Rolling, sliding and torsion of micron-sized silica particles: experimental, numerical and theoretical analysis. *Granular matter*, 16(3):281–297.

Guillard, F., Marks, B., and Einav, I. (2017). Dynamic x-ray radiography reveals particle size and shape orientation fields during granular flow. *Scientific Reports*, 7.

Hanes, D. M. and Inman, D. L. (1985). Observations of rapidly flowing granular-fluid materials. *Journal of Fluid Mechanics*, 150:357–380.

Hatano, T. (2007). Power-law friction in closely packed granular materials. *Physical Review E*, 75(6):060301.

Howell, D., Behringer, R., and Veje, C. (1999). Stress fluctuations in a 2d granular couette experiment: a continuous transition. *Physical Review Letters*, 82(26):5241.

Hungr, O. and Morgenstern, N. (1984). High velocity ring shear tests on sand. *Géotechnique*, 34(3):415–421.

Hvorslev, M. J. (1936). A ring shearing apparatus for the determination of the shearing resistance and plastic flow of soil. In *Proceedings of the 1st International Conference on Soil Mechanics and Foundation Engineering*, pages 125–129, Harvard University. Graduate School of Engineering, Harvard University.

Hvorslev, M. J. (1939). Torsion shear tests and their place in the determination of the shearing resistance of soils. In *Proceedings-American Society for Testing and Materials*, volume 39, page 999, Philadelphia. American Society for Testing and Materials.

Iordanoff, I. and Khonsari, M. (2004). Granular lubrication: toward an understanding of the transition between kinetic and quasi-fluid regime. *Journal of Tribology*, 126(1):137–145.

Jop, P., Forterre, Y., and Pouliquen, O. (2005). Crucial role of sidewalls in granular surface flows: consequences for the rheology. *Journal of Fluid Mechanics*, 541:167–192.

Jop, P., Forterre, Y., and Pouliquen, O. (2006). A constitutive law for dense granular flows. *Nature*, 441(7094):727–730.

Kamrin, K. and Koval, G. (2012). Nonlocal constitutive relation for steady granular flow. *Physical Review Letters*, 108(17):178301.

Kelly, R., Airey, D. W., and Tabucanon, J. (2003). Design and performance of a 1m diameter ring shear apparatus. *Geotechnical Testing Journal*, 26(4):444–449.

Khosropour, R., Zirinsky, J., Pak, H., and Behringer, R. (1997). Convection and size segregation in a couette flow of granular material. *Physical Review E*, 56(4):4467.

Koval, G., Roux, J.-N., Corfdir, A., and Chevoir, F. (2009). Annular shear of cohesionless granular materials: From the inertial to quasistatic regime. *Physical Review E*, 79(2):021306.

Larsen, I. J., Montgomery, D. R., and Korup, O. (2010). Landslide erosion controlled by hillslope material. *Nature Geoscience*, 3(4):247.

Losert, W., Bocquet, L., Lubensky, T., and Gollub, J. P. (2000). Particle dynamics in sheared granular matter. *Physical Review Letters*, 85(7):1428.

Marks, B., Sandnes, B., Dumazer, G., Eriksen, J. A., and Måløy, K. J. (2015). Compaction of granular material inside confined geometries. *Frontiers in Physics*, 3:41.

MiDi, G. (2004). On dense granular flows. *The European Physical Journal E*, 14(4):341–365.

Open Geomechanics, 2022, article no. 2

Yang Liu, François Guillard, Benjy Marks, Pierre Rognon & Itai Einav, *The perpetual shearing of granular soils under low stresses using the stadium shear device*

17

Miller, B., O'Hern, C., and Behringer, R. (1996). Stress fluctuations for continuously sheared granular materials. *Physical Review Letters*, 77(15):3110.

Miller, T., Rognon, P., Metzger, B., and Einav, I. (2013). Eddy viscosity in dense granular flows. *Physical Review Letters*, 111(5):058002.

Mitchell, J., Houston, W., Scott, R., Costes, N., Carrier III, W., and Bromwell, L. (1972). Mechanical properties of lunar soil: Density, porosity, cohesion and angle of internal friction. In *Lunar and Planetary Science Conference Proceedings*, volume 3, page 3235, Cambridge. Cambridge University Press, Cambridge.

Morrow, C. A. and Byerlee, J. D. (1989). Experimental studies of compaction and dilatancy during frictional sliding on faults containing gouge. *Journal of Structural Geology*, 11(7):815–825.

Mueth, D. M., Debregeas, G. F., Karczmar, G. S., Eng, P. J., Nagel, S. R., and Jaeger, H. M. (2000). Signatures of granular microstructure in dense shear flows. *Nature*, 406(6794):385–389.

Negussey, D., Wijewickreme, W., and Vaid, Y. (1988). Constant-volume friction angle of granular materials. *Canadian Geotechnical Journal*, 25(1):50–55.

Novosad, J. (1964). Studies on granular materials. ii. apparatus for measuring the dynamic angle of internal and external friction of granular materials. *Collection of Czechoslovak Chemical Communications*, 29(11):2697–2701.

Omidvar, M., Iskander, M., and Bless, S. (2012). Stress-strain behavior of sand at high strain rates. *International Journal of Impact Engineering*, 49:192–213.

Peyneau, P.-E. and Roux, J.-N. (2008). Frictionless bead packs have macroscopic friction, but no dilatancy. *Physical Review E*, 78(1):011307.

Rankine, W. M. (1857). On the stability of loose earth. *Philosophical Transactions of the Royal Society of London*, 147:9–27.

Rognon, P., Miller, T., and Einav, I. (2015a). A circulation-based method for detecting vortices in granular materials. *Granular Matter*, 17(2):177–188.

Rognon, P. G., Miller, T., Metzger, B., and Einav, I. (2015b). Long-range wall perturbations in dense granular flows. *Journal of Fluid Mechanics*, 764:171–192.

Rood, K. M. (1984). *An aerial photograph inventory of the frequency and yield of mass wasting on the Queen Charlotte Islands, British Columbia*. Information Services Branch, Ministry of Forests.

Rousé, P. C. (2018). Relation between the critical state friction angle of sands and low vertical stresses in the direct shear test. *Soils and Foundations*, 58(5):1282–1287.

Rowe, P. W. (1962). The stress-dilatancy relation for static equilibrium of an assembly of particles in contact. *Proceedings of the Royal Society of London A: Mathematical, Physical and Engineering Sciences*, 269(1339):500–527.

Sassa, K. (1997). A new intelligent-type dynamic loading ring shear apparatus. *Landslide News*, 10:33.

Savage, S. and Sayed, M. (1984). Stresses developed by dry cohesionless granular materials sheared in an annular shear cell. *Journal of Fluid Mechanics*, 142:391–430.

Savage, S. B. (1984). The mechanics of rapid granular flows. *Advances in Applied Mechanics*, 24:289–366.

Schanz, T. and Vermeer, P. (1996). Angles of friction and dilatancy of sand. *Géotechnique*, 46(1):145–152.

Schofield, A. and Wroth, P. (1968). *Critical state soil mechanics*, volume 310. McGraw-Hill London, London.

Simoni, A. and Houlsby, G. T. (2006). The direct shear strength and dilatancy of sand–gravel mixtures. *Geotechnical & Geological Engineering*, 24(3):523.

Srivastava, I., Silbert, L. E., Grest, G. S., and Lechman, J. B. (2021). Viscometric flow of dense granular materials under controlled pressure and shear stress. *Journal of Fluid Mechanics*, 907:A18.

Standards Australia (1998). Soil compaction and density tests - determination of the minimum and maximum dry density of a cohesionless material - standard method. Standard, Standards Australia Limited, Sydney.

Sun, X., Kob, W., Blumenfeld, R., Tong, H., Wang, Y., and Zhang, J. (2020). Friction-controlled entropy-stability competition in granular systems. *Physical Review E*, 125(26):268005.

Tabucanon, J. T. (1997). *Shaft resistance of piles in sand*. PhD thesis, The University of Sydney.

Tatsuoka, F., Sakamoto, M., Kawamura, T., and Fukushima, S. (1986). Strength and deformation characteristics of sand in plane strain compression at extremely low pressures. *Soils and Foundations*, 26(1):65–84.

Tengattini, A., Das, A., and Einav, I. (2016). A constitutive modelling framework predicting critical state in sand undergoing crushing and dilation. *Géotechnique*, 66(9):695–710.

Thornton, A., Weinhart, T., Luding, S., and Bokhove, O. (2012). Modeling of particle size segregation: calibration using the discrete particle method. *International Journal of Modern Physics C*, 23(08):1240014.

Tian, Y. and Cassidy, M. J. (2008). Modeling of pipe–soil interaction and its application in numerical simulation. *International Journal of Geomechanics*, 8(4):213–229.

Tika, T. E. and Hutchinson, J. (1999). Ring shear tests on soil from the vaiont landslide slip surface. *Géotechnique*, 49(1):59–74.

Tika, T. E., Vaughan, P., and Lemos, L. (1996). Fast shearing of pre-existing shear zones in soil. *Géotechnique*, 46(2):197–233.

Toyota, H., Nakamura, K., Sugimoto, M., and Sakai, N. (2009). Ring shear tests to evaluate strength parameters in various remoulded soils. *Géotechnique*, 59(8):649–659.

Vaid, Y. and Sasitharan, S. (1992). The strength and dilatancy of sand. *Canadian Geotechnical Journal*, 29(3):522–526.

Veje, C., Howell, D. W., and Behringer, R. (1999). Kinematics of a two-dimensional granular couette experiment at the transition to shearing. *Physical Review E*, 59(1):739.

Weinhart, T., Thornton, A. R., Luding, S., and Bokhove, O. (2012). From discrete particles to continuum fields near a boundary. *Granular Matter*, 14(2):289–294.

White, D. J., Randolph, M. F., et al. (2007). Seabed characterisation and models for pipeline-soil interaction. *International Journal of Offshore and Polar Engineering*, 17(03).

Open Geomechanics, 2022, article no. 2
Yang Liu, François Guillard, Benjy Marks, Pierre Rognon & Itai Einav, *The perpetual shearing of granular soils under low stresses using the stadium shear device*

18

Wilford, D. and Schwab, J. (1982). Soil mass movements in the rennell sound area, queen charlotte islands, british columbia. In *Proceedings of the Canadian Hydrology Symposium-Associate Committee on Hydrology*, pages 521–541, Ottawa. National Research Council of Canada.

Wood, D. M. (1990). *Soil behaviour and critical state soil mechanics*. Cambridge University Press, Cambridge, Cambridge.

Zhang, J., Stewart, D. P., and Randolph, M. F. (2002). Modeling of shallowly embedded offshore pipelines in calcareous sand. *Journal of Geotechnical and Geoenvironmental engineering*, 128(5):363–371.